Mon. Not. R. Astron. Soc. **279,** 1197–1209 (1996)

Observations of the radio jets in NGC 5090 (PKS B1318 – 434)

B. D. Lloyd,[1] P. A. Jones[1] and R. F. Haynes[2]

[1]*Physics Department, University of Western Sydney Nepean, P.O. Box 10, Kingswood 2747, NSW, Australia*
[2]*Australia Telescope National Facility, P.O. Box 76, Epping, NSW 2121, Australia*

Accepted 1995 November 1. Received 1995 October 30; in original form 1995 August 7

ABSTRACT

We present results from Australia Telescope Compact Array (ATCA) observations, at 4.796 and 8.640 GHz, of the Fanaroff–Riley class I, extragalactic radio jets in the galaxy NGC 5090 (PKS B1318 – 434). This radio galaxy is relatively close, $z = 0.011$, and may be evolving under the influence of a nearby galaxy, NGC 5091. Total intensity and polarization radio images of these jets are used to determine the magnetic field structure, fractional polarization, spectral index and depolarization variations along the jets. Mach numbers of 1–3 and velocities of 2000–15 000 km s^{-1} along the jets are implied, with velocities of 0.05–0.2 times the speed of light where the jets initially flare.

Key words: galaxies: individual: NGC 5090 – galaxies: jets – galaxies: structure – radio continuum: galaxies.

1 INTRODUCTION

The radio source PKS B1318 – 434 was first identified with the elliptical galaxy NGC 5090 by Ekers (1969). It has been an object of interest because of its association and possible interaction with the nearby edge-on spiral galaxy NGC 5091. This idea is currently supported by the following circumstantial evidence: the disturbed and brightened spiral arm in NGC 5091 (first noted by Bergwall et al. 1978) which may be caused by tidal interaction with the elliptical galaxy; NGC 5090 and 5091 have a redshift difference of 245 km s^{-1} and a projected separation of 70 arcsec or approximately 12 h^{-1} kpc (we use $H_0 = 100\ h$ km s^{-1} Mpc^{-1} throughout this paper); NGC 5090 produces two large-scale radio jets with the radio axis perpendicular to the line connecting the two galactic nuclei (first noted by Schilizzi & McAdam 1975; Schilizzi 1975). This suggests that tidal interaction from the spiral galaxy may be influencing the way in which the central engine of the elliptical is fuelled. A detailed optical and radio study of the system was carried out by Smith & Bicknell (1986, hereafter SB) with the Anglo-Australian Telescope, the Fleurs Synthesis Telescope (FST) and the Molonglo Synthesis Telescope (MOST). They suggested that the tidal interaction of NGC 5091 with NGC 5090 may enhance fuelling of the central engine of NGC 5090 via an inner Lindblad resonance which produces jets that travel perpendicularly to the orbital plane of NGC 5091. As PKS B1318 – 434 lies behind the southern lobe of Centaurus A, the dynamic range of the MOST and FST images was limited by the bright jets and core of Centaurus A. Properties of NGC 5090 are shown in Table 1 and are derived from SB, Schilizzi & McAdam (1975), Cooper, Price & Cole (1965), Jones & McAdam (1992) and Junkes et al. (1993).

2 OBSERVATIONS

We observed PKS B1318 – 434 with the Australia Telescope Compact Array (ATCA) in three 12-h observations during 1993, using a total of 45 baselines from the 1.5A, 1.5B and 6.0C configurations. We used the dual-frequency continuum mode, observing with a 128-MHz bandwidth centred on 4.796 and 8.640 GHz. The broad-scale structure and full extent of the radio source (17×5 arcmin^2) were covered by time sharing between three pointing centres when using the 1.5-km arrays (see Table 2). The full 12-hr synthesis observation, with the 6.0C array, was spent on the central region so that high-resolution images could be made of the jets close to the core.

3 DATA REDUCTION AND IMAGING

The data were edited using the AIPS software package, then transferred to MIRIAD for full polarimetric calibration and imaging. We use the revised flux densities of the primary calibrator 1934 – 638 of 5.83 Jy at 4.796 GHz and 2.84 Jy at 8.640 GHz to correct the flux scale (Reynolds, private communication). The calibrator source at 1313 – 33 was observed over a wide range of parallactic angles to correct for instrumental and environmental antenna gain and phase

fluctuations during the observations. Imaging was carried out in MIRIAD using the SDI CLEAN algorithm. Initially, CLEAN components were selected only from regions known to contain emission from the radio source. These CLEANing regions were adjusted so that the side-lobes were minimized in the residual image. CLEAN components were then selected from the whole imaging field. Atmospheric phase errors were corrected with a few self-calibration iterations using CLEAN components from the core, and the field re-imaged. Images from each pointing centre were obtained and self-calibrated separately in order to maximize the dynamic range, and were finally corrected for primary beam attenuation.

3.1 Total intensity

The (u,v) data were tapered before imaging to give images at three different resolutions (16-, 8- and 4-arcsec circular restoring beams), to show the low surface brightness structure of the lobes and the narrow jets near the core. Throughout this paper we use I_ν to denote surface brightness, Θ to denote the angular distances from the core, and Φ to denote the jet full width to half-maximum.

Fig. 1 shows the total intensity image of PKS B1318 – 434 at 4.796 GHz with a resolution of 16 arcsec, and was made by combining images at the three pointing centres. The radio source is approximately 17 arcmin (167 h^{-1} kpc) in total extent. There is a strong core component from which two bright jets originate. Overall, the surface brightness appears asymmetric about the core. Both jets exhibit large-scale transverse deviations which have an 'S' inversion symmetry about the core. These sinusoidal deviations continue into the lobes and are a dominant feature in the structure of the radio source as a whole.

Table 1. Summary of properties of NGC 5090 and integral properties of PKS B1318 – 434. The spectral index is defined as $I_\nu \propto \nu^\alpha$.

Optical position RA (J2000)	$13^h\ 21^m\ 12\overset{s}{.}7$
Optical position Dec. (J2000)	$-43°\ 42'\ 16''$
Morphological type	E2
Redshift	0.01129
Angular scale	164 h^{-1} pc arcsec^{-1}
Total blue magnitude	12.6
408 MHz flux density	10.0 Jy
843 MHz flux density	7.16 Jy
1.41 GHz flux density	5.8 Jy
4.75 GHz flux density	3.03 Jy
Total spectral index	-0.6
1.41 GHz luminosity	7.1×10^{23} h^{-2} W Hz^{-1}
10 MHz to 100 GHz radio luminosity	1.4×10^{34} h^{-2} W

The north-eastern jet rapidly widens and brightens into a large bright spot in the first 2 arcmin (20 h^{-1} kpc) from the core. It then narrows before entering a diffuse elongated lobe which extends out to $\Theta \simeq 8$ arcmin (79 h^{-1} kpc).

The south-western jet is initially brighter than its counterpart and maintains approximately constant surface brightness for the first 2 arcmin (20 h^{-1} kpc). As the jet enters the bright southern lobe, the peak flux ridge line swings southward and then splits into two distinct ridges at $\Theta = 3$ arcmin (30 h^{-1} kpc). One ridge line curls around toward the east and 0.5 arcmin back towards the core; the other bends back to the south-west where the emission becomes diffuse and elongated; the emission terminates at $\Theta \simeq 9$ arcmin (89 h^{-1} kpc).

At 8-arcsec (1.3 h^{-1} kpc) resolution, the total intensity contours (Fig. 2) show the structure of each jet over the first 3 arcmin from the core. The 'S'-shaped transverse deviations and asymmetric fluctuations in the total intensity along the jets are prominent features in this image. Over the first 45 arcsec the surface brightness of the south-western jet is strong, but it declines in the following 1 arcmin. Conversely, the north-eastern jet is not as bright over the first 45 arcsec, but brightens markedly over the following 1 arcmin and then fades quickly as it merges into the lobe.

At our highest observing resolution of 4 arcsec (0.7 h^{-1} kpc), Fig. 3 shows the total intensity contours at 4.796 GHz, over the first 2 arcmin from the core. The knotty structure of the inner jets is clearly seen. At angular distances less than 12 arcsec (2.0 h^{-1} kpc) from the core, the north-eastern jet is faint and unresolved; it then flares, initiating a series of knots. The jet is not seen in the south-western arm at angular distances less than 12 arcsec from the core; the jet 'turns on' after this point and there are a number of unresolved and partially resolved knots along the bright inner part of the jet, which terminate at $\Theta = 2$ arcmin.

3.2 Fractional polarization

The fractional polarization or degree of linear polarization is defined as $m_L = I_P/I$, where the linearly polarized intensity is $I_P = \sqrt{Q^2 + U^2}$ and the polarization position angle $\chi = (1/2)$ arctan (U/Q) for Stokes parameters I, Q and U.

Fig. 1 also shows the projected magnetic field vectors; the degree of linear polarization is indicated by the length of the vectors. At the base of each jet, $\Theta < 0.5$ arcmin, the fractional polarization is less than 10 per cent. Moving along the jets, toward the lobes, the amount of fractional polarization fluctuates but gradually increases.

The fractional polarization in both jets increases to 10–30 per cent at angular distances of $0.5 < \Theta < 1.5$ arcmin, and has several maxima in polarization knots along the jets, except along the eastern side of the bright region in the

Table 2. Pointing centres used for the ATCA observations.

Pointing Centre	RA (J2000)	Dec. (J2000)	Observation time (hours)
North	$13^h\ 21^m\ 20\overset{s}{.}4$	$-43°\ 36'\ 42''$	8
Central	$13^h\ 21^m\ 15\overset{s}{.}5$	$-43°\ 42'\ 12''$	16
South	$13^h\ 20^m\ 50\overset{s}{.}4$	$-43°\ 46'\ 43''$	8

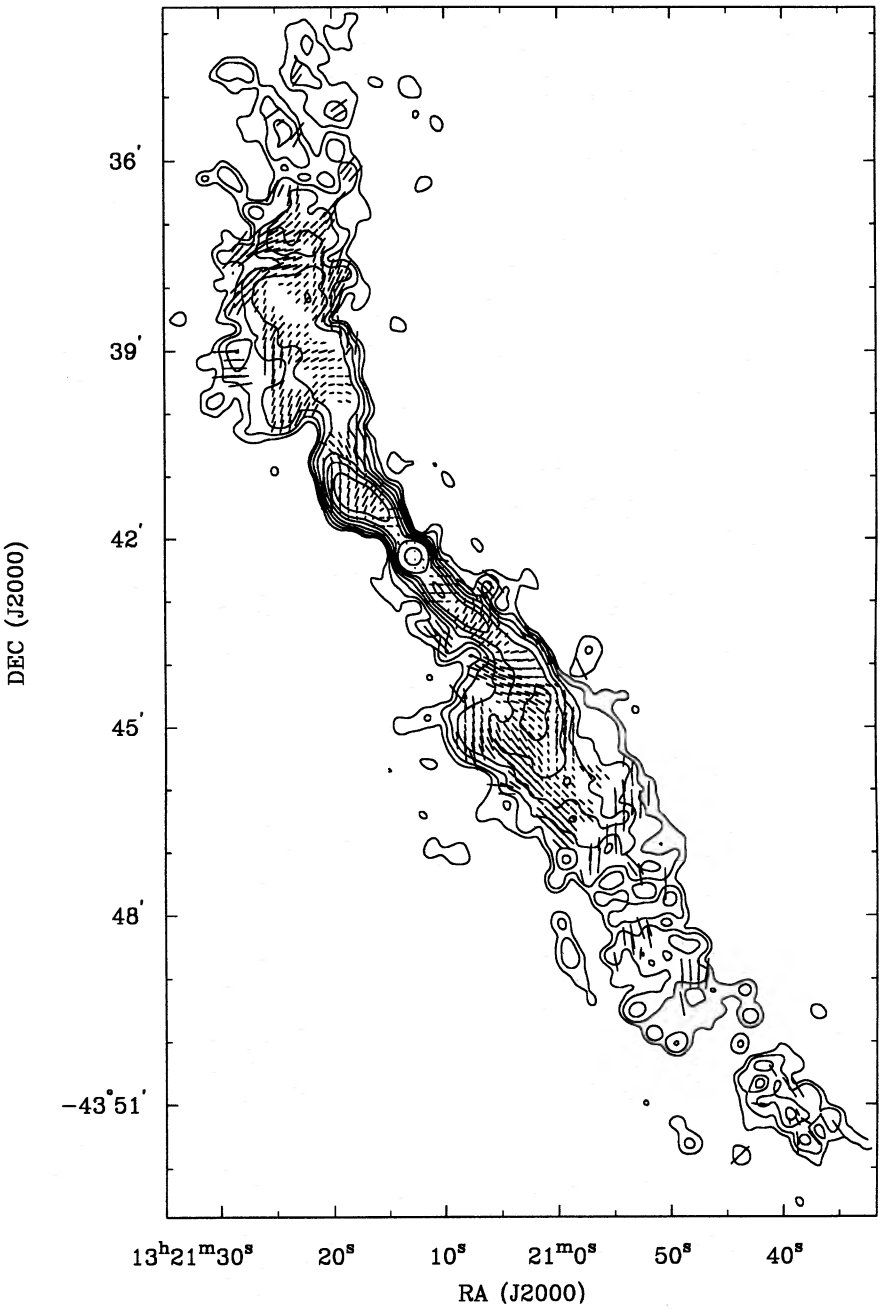

Figure 1. The 4.796-GHz, 16 arcsec resolution image of the projected magnetic field vectors overlaid on total intensity contours. Contours are at 0.2, 0.4, 0.8, 1.5, 3, 5, 10 and 50 per cent of the peak core flux of 530 mJy per beam. The length of the vectors represents the degree of linear polarization, where a vector length of 1 arcsec corresponds to 2.6 per cent fractional polarization.

northern jet, $\Theta \simeq 2$ arcmin, where it reaches a maximum of about 40–50 per cent.

Fractional polarization in the southern lobe is greatest along the north-eastern and western sides, and has a maximum of $\sim$50 per cent along the south-eastern side of the lobe, 2.5 arcmin from the core. The amount of fractional polarization in the northern lobe is, in general, much less than in the south-western lobe, typically 10–30 per cent.

Fractional polarization in the 8 and 4 arcsec resolution images is better illustrated as SLICE plots (see Section 4.3.4). The rms noise levels in the 4 and 8 arcsec resolution polarized intensity images are 60 and 90 μJy beam^{-1} respectively.

3.3 Magnetic field structure

The projected magnetic field vectors in our 16 arcsec resolution image are shown in Fig. 1. The vectors have not been corrected for Faraday rotation, although, from rotation measurements in the jets (see Section 4.3.7), we expect that Faraday rotation contributes at most 10°–15° to the position angle of the vectors at this frequency.

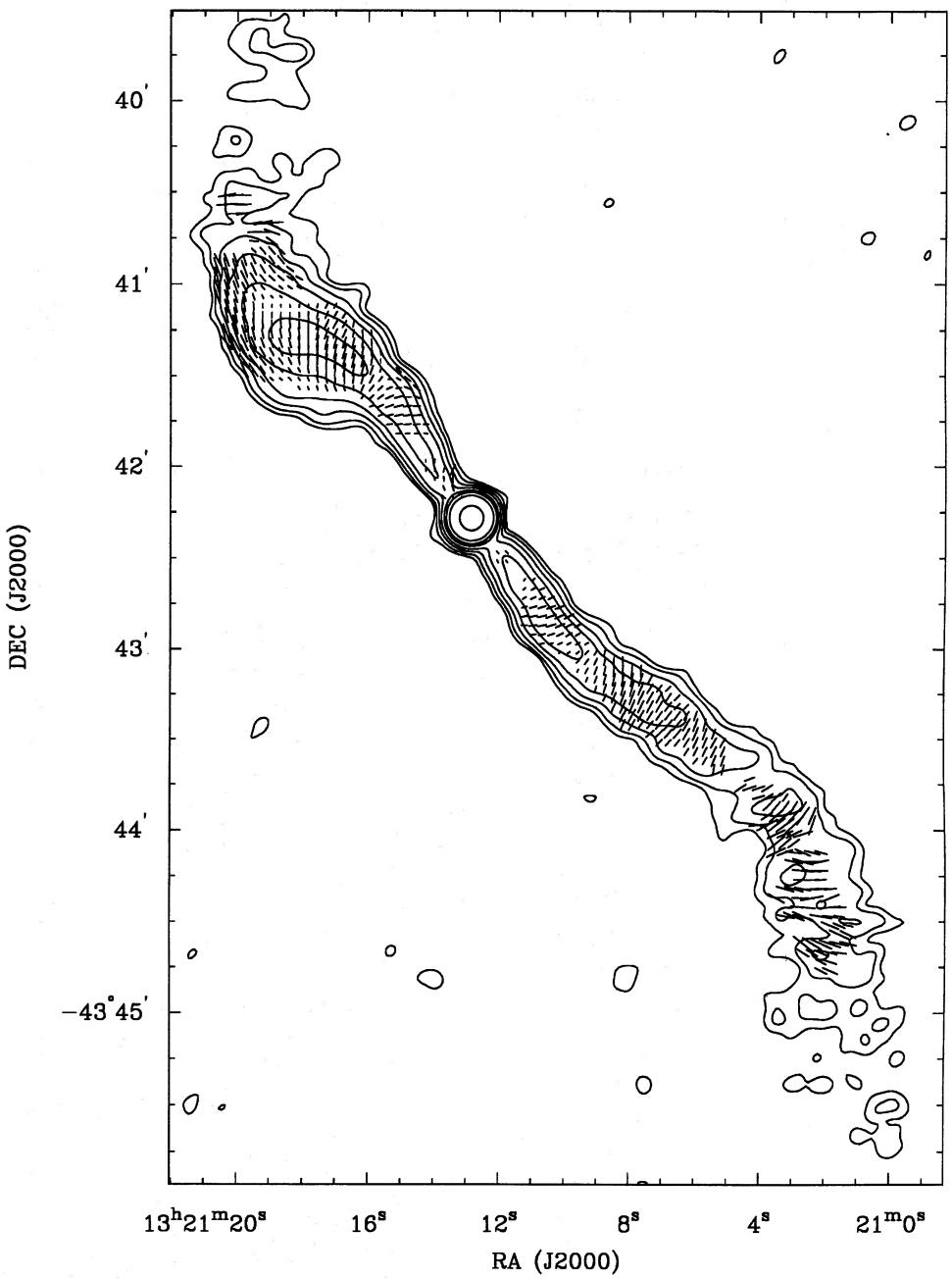

Figure 2. The 4.796-GHz, 8 arcsec resolution image of the projected magnetic field vectors, corrected for Faraday rotation, overlaid on total intensity contours. Contour levels are at 0.2, 0.4, 0.8, 1.5, 3, 5, 10 and 50 per cent of the peak core flux of 530 mJy per beam. The length of the vectors represents the degree of linear polarization, where a vector length of 1 arcsec represents 7.5 per cent fractional polarization. The rms noise is 0.3 mJy per beam, corresponding to a dynamic range of 1800:1.

In the south-western jet the magnetic field lines are slightly oblique over the first arcminute ($9.8\,h^{-1}$ kpc); they become perpendicular to the jet thereafter. The magnetic field lines remain perpendicular to the peak flux ridge line as it enters the lobe, and curve around to the south-west, where they are aligned along the sides of the lobe.

The projected magnetic field lines in the north-eastern jet are initially oblique to the ridge line for $\Theta \leq 1$ arcmin. At greater angular distances along the jet, the vectors rotate anticlockwise with respect to the peak flux ridge line until they are parallel at the end and on the outside bend of the bright spot in the jet at $\Theta = 1.5$ arcmin. They continue to rotate anticlockwise just before entering the northern lobe where they are again perpendicular to the ridge line. The field lines in the lobe remain perpendicular to the peak flux ridge line and are aligned with the sides of the lobe.

Fig. 2 shows the magnetic field structure, corrected for Faraday rotation, in the jets with 8-arcsec resolution. Some of the more complex features seen in the 16 arcsec resolution image can now be seen in more detail. At the base of both jets ($\Theta < 0.5$ arcmin) the vectors are parallel to the peak flux ridge line. After this point, the magnetic field lines

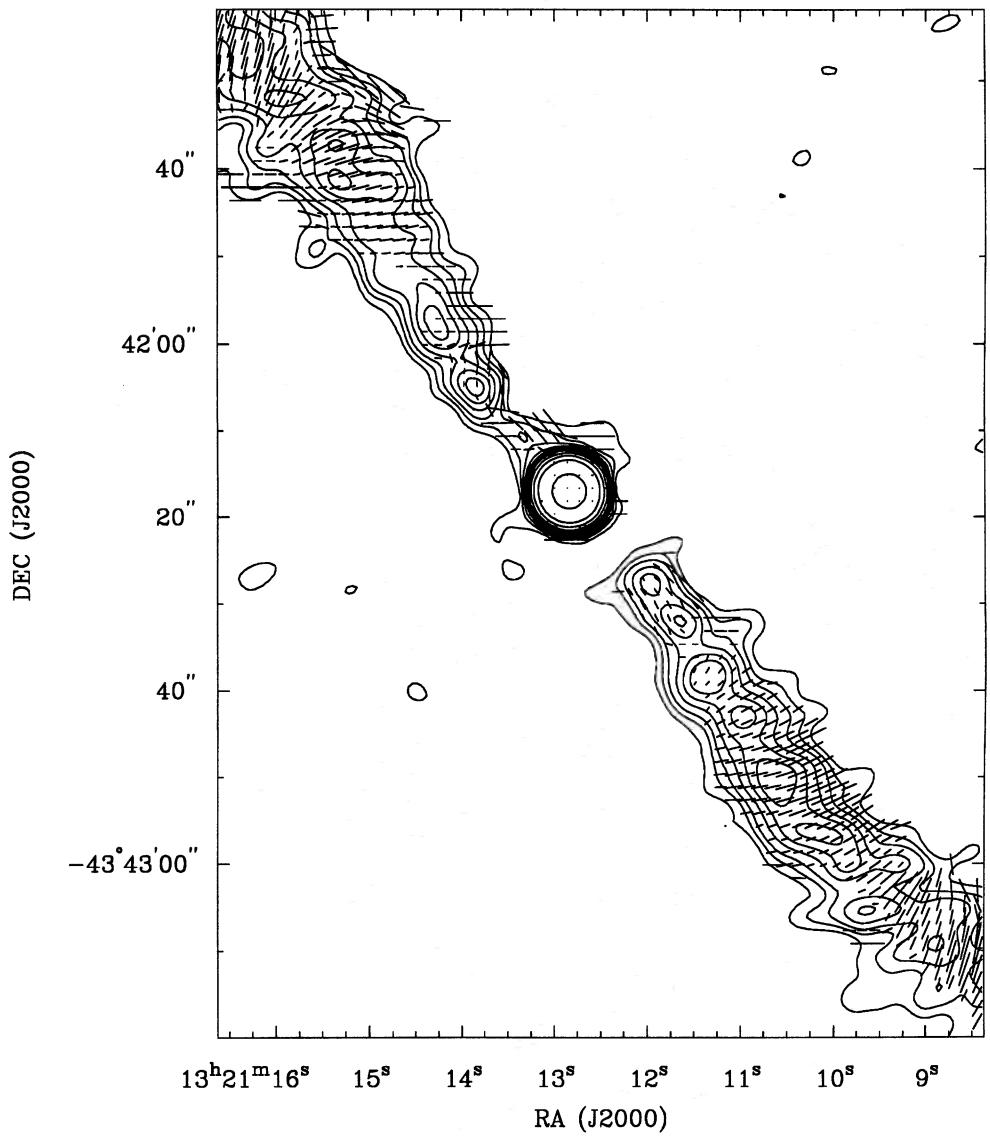

Figure 3. The 4.796-GHz, 4 arcsec resolution image of the projected magnetic field vectors overlaid on total intensity contours. Contour levels are at 0.2, 0.4, 0.6, 0.9, 1.2, 1.5, 2, 3, 5, 10 and 50 per cent of the peak core flux of 532 mJy per beam. The length of the vectors represents the degree of linear polarization, where a vector length of 1 arcsec represents 11 per cent fractional polarization. The rms noise is 0.4 mJy per beam, corresponding to a dynamic range of 1300:1.

remain perpendicular to the ridge line. A departure from this magnetic field configuration is seen in the north-eastern jet along the outside of bends in the jet: namely, at $\Theta = 45$ arcsec and at $\Theta = 1.5$ arcmin the projected magnetic field lines are aligned with the sides of the jet. Associated with the latter, there is a sharp kink in the peak fractional polarization ridge line along the jet. This ridge line follows the bend in the peak flux ridge line, but is more pronounced. The magnetic field lines are aligned with the sides where the fractional polarization is greatest.

The south-western jet does not show such contrasts in magnetic field structure. The projected magnetic field vectors are predominantly perpendicular to the peak flux ridge line. The field lines appear slightly more oblique to the ridge line along the edges.

Our 4 arcsec resolution image, Fig. 3, shows the projected magnetic field vectors, corrected for Faraday rotation, of both jets up to angular distances of 1 arcmin from the core.

The magnetic field lines are parallel to the faint unresolved part of the north-eastern jet before it flares. The field lines are directed around the first knot, over the range $15 < \Theta < 20$ arcsec (2.5–3.3 h^{-1} kpc), they are oblique across the second knot, $20 < \Theta < 30$ arcsec (3.3–4.9 h^{-1} kpc), and they gradually rotate to become perpendicular to the jet at angular distances greater than 30 arcsec (4.9 h^{-1} kpc). An important feature to note is that the jet is polarized to a greater degree on the western side at distances up to $\Theta = 35$ arcsec (5.7 h^{-1} kpc).

In the south-western jet the magnetic field vectors are

parallel to the peak flux ridge line over the first two knots, $12<\Theta<25$ arcsec (2.0–4.1 h^{-1} kpc). They are perpendicular to the peak flux ridge line and slightly oblique along the sides of the train of knots, in the range $25<\Theta<55$ arcsec (4.1–9.0 h^{-1} kpc), and remain perpendicular to the peak flux ridge line at greater angular distances.

4 SOURCE PROPERTIES

4.1 Core properties

The core properties are summarized in Table 3. Flux density measurements of the core were made from our highest resolution (4 arcsec) images, so that no flux from the jets was included. The core position was determined from images that had not been self-calibrated, as self-calibration in phase yields unreliable absolute positions (usually by a few arcseconds). The core spectral index is inverted, $\alpha=+0.2$ (where we use $S_\nu \propto \nu^\alpha$). The core is less than 1 per cent polarized at 4.796 and 8.640 GHz. The values of spectral index agree with those of the FST and MOST images (SB; Jones & McAdam 1992), and with the PTI core flux data (Jones, McAdam & Reynolds 1994; Slee et al. 1994).

4.2 Lobe properties

The physical properties and equipartition parameters (Pacholczyk 1970) of the lobes are summarized in Table 4. The spectral variations across the lobes are uncertain, although we assume a spectral index of $\alpha=-0.9$ as measured by Wall & Schilizzi (1979) in each lobe when calculating the integral and equipartition properties.

4.3 Jet properties

To study the properties of the jets in an analytical fashion, a one-dimensional Gaussian was fitted to each transverse profile along the jets and the peak flux, I, full width at half-maximum, FWHM or Φ, and transverse peak position determined as a function of angular distance from the core. These quantities were used to determine the spreading rate, peak flux, spectral index, fractional polarization, depolarization and equipartition parameters up to angular distances of 3 arcmin from the core. The true jet FWHM was determined by deconvolving it with the CLEAN beam, and is given by $\Phi_{decv}=(\Phi^2_{obs}-\Phi^2_{beam})^{1/2}$ where Φ_{obs} and Φ_{beam} are the observed and synthesized beam FWHM respectively. The deconvolved peak flux is given by $I_{decv}=I_{obs}(\Phi^2_{beam}/\Phi^2_{decv}+1)^{1/2}$ where I_{obs} is the observed peak flux density (see Fig. 4).

4.3.1 *Spreading rate*

The variations in jet FWHM along the jets as a function of angular distance from the core have been determined using data from total intensity images at all three resolutions. The spreading rate is low compared with that of a 'free' jet; both jets typically have $d\Phi/d\Theta=0.20\pm0.02$, but the northern jet rapidly expands in the region $55<\Theta<75$ arcsec from the core, where the spreading rate reaches up to 0.65 ± 0.09. If the jet is twisting and overlapping in projection, the observed jet FWHM will not be a true measure of the jet width. This effect is probably seen in the rapid broadening and then contraction of the northern jet in this region.

4.3.2 *The I_ν–Φ relation*

The relationship between the jet surface brightness and width is a simple but important diagnostic in analysing the dynamics of the jet. For an adiabatically expanding laminar flow jet, the relation is of the form $I_\nu \propto \Phi^x$, where x depends on the spectral index and magnetic field configuration (see Section 5.4). In the north-eastern jet ($25<\Theta<60$ arcsec, Fig. 5), the surface brightness remains fairly constant with increasing width; in the range $60<\Theta<100$ arcsec the jet brightens and rapidly expands, and then contracts. For angular distances $100<\Theta<120$ arcsec the relation is $I_\nu \propto \Phi^{-1.5}$, and is not well defined for the remainder of the jet. There are large non-linear deviations from a smooth curve, usually associated with knots and areas of the jet that may be twisting so that projection effects will increase the observed jet width and surface brightness. The I_ν–Φ plot for the south-western jet shows a similar deviation associated with the bright lobe, but generally obeys the relation $I_\nu \propto \Phi^{-1.5}$ for $25<\Theta<80$ arcsec.

Table 3. Core properties.

RA (J2000)	$13^h\ 21^m\ 12\overset{s}{.}8$
Dec. (J2000)	$-43°\ 42'\ 17''$
Flux Density at 4.796 GHz	0.53 Jy
Flux Density at 8.640 GHz	0.58 Jy
Spectral Index	+0.15
Luminosity at 4.796 GHz	6.5×10^{22} h^{-2} W Hz^{-1}

Table 4. Lobe properties.

Lobe Property at 4.796 GHz	Northern Lobe	Southern Lobe
Flux Density (Jy)	0.60	1.00
Luminosity (h^{-2} W Hz^{-1})	7.2×10^{22}	1.2×10^{23}
Total Luminosity (h^{-2} W)	2.8×10^{33}	4.7×10^{33}
Equipartition parameters		
Minimum total energy (h$^{-17/7}$ W)	1.4×10^{50}	1.9×10^{50}
Minimum energy density (h$^{-4/7}$ J m^{-3})	9.2×10^{-14}	1.2×10^{-13}
Minimum magnetic field strength (h$^{-2/7}$ T)	2.8×10^{-10}	3.3×10^{-10}
Minimum pressure (h$^{-4/7}$ Pa)	4.9×10^{-14}	6.6×10^{-14}

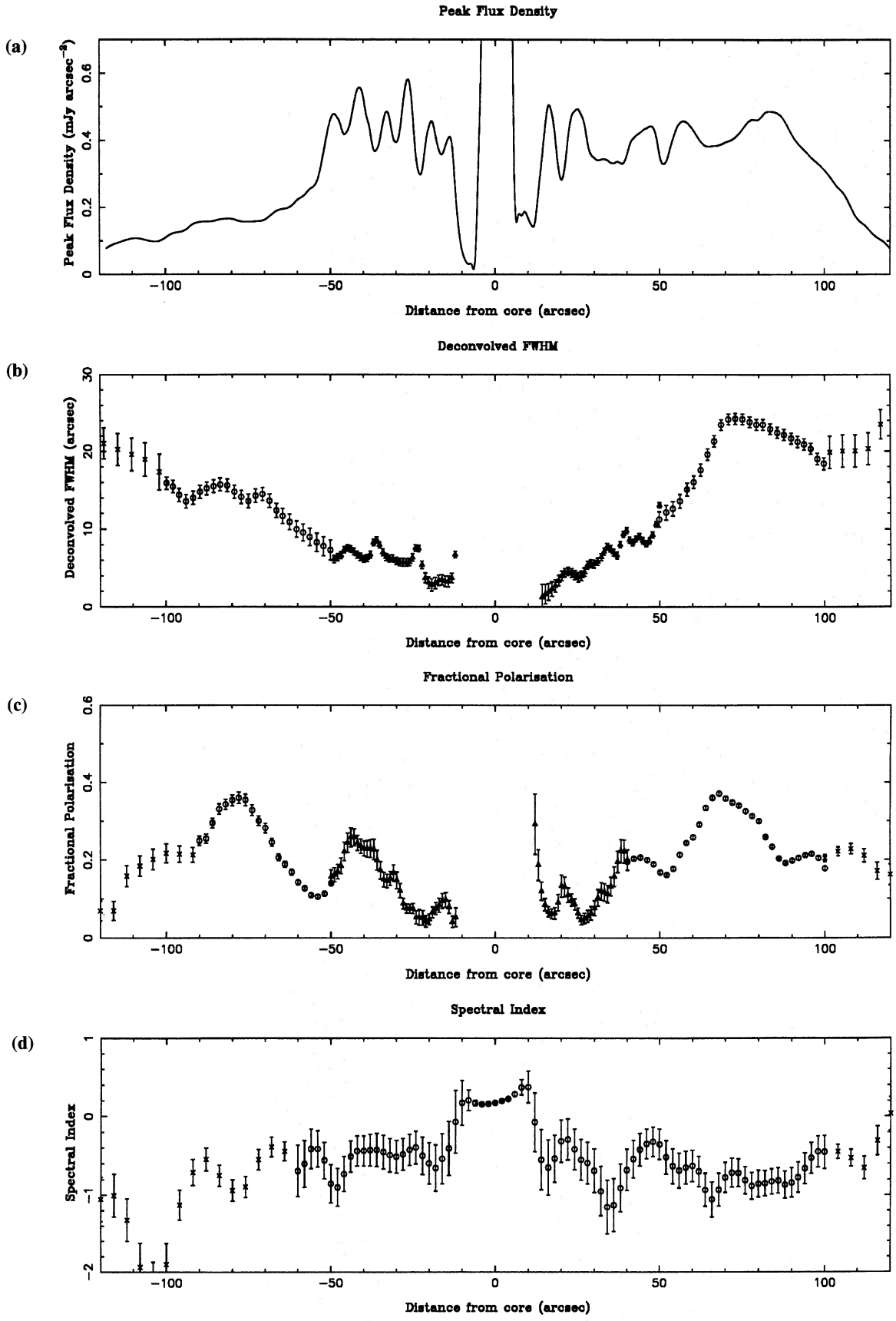

Figure 4. (a) The peak flux density, (b) the deconvolved FWHM, (c) the fractional polarization and (d) the spectral index along the northern jet (positive angular distances from the core) and southern jet (negative angular distances from the core). The crosses are derived from the 16-arcsec images, the circles from the 8-arcsec images and the solid triangles from the 4-arcsec images.

© 1996 RAS, MNRAS **279**, 1197–1209

4.3.3 *Spectral index*

Our data show no detectable spectral variations across the jets, so we consider only the variations along the peak flux ridge line of the jet. The spectral index along the jets is shown in Fig. 4(d). Although the formal errors are shown, care must be taken when interpreting the spectral index variations, as images at the two frequencies have been made with different (u,v) coverage and therefore the results are highly dependent on the quality of interpolated missing (u,v) data points.

There appears to be a correlation between fluctuations in the ridge line peak flux density (Fig. 4a) and the spectral index along the jets. Flatter spectral indices are associated with the regions of the jet on or just after knots; the spectral index steepens along the jet before reaching the next knot. The spectral index also flattens just before entering the lobes.

4.3.4 *Fractional polarization*

The degree of linear polarization is shown in Fig. 4(c). The fractional polarization along the jet exhibits large variations. Comparing the fractional polarization with the ridge line peak flux, the fractional polarization is greater just before a knot and lower following the knot, and increases towards the next knot. The fractional polarization increases in the 're-collimation shoulders', just before entering the lobes.

4.3.5 *Transverse deviations*

Fig. 6 shows the transverse deviations of the peak flux ridge line along the radio axis relative to position angle 41°. The amplitude, A, increases linearly with $A=(0.10\pm0.01)\Theta$ over the first 3 arcmin from the core, but does not have a constant wavelength. At angular distances of $\Theta<28$ arcsec the wavelength of these deviations, λ, is small in both jets. The deviations of both jets increase in wavelength at angular distances $28<\Theta<100$ arcsec; λ decreases just before entering the lobes. The transverse deviations and the parameter λ/R (where R is the mean jet radius) are useful in the analysis of jet instabilities (see Section 5.6.1). The parameter λ/R is shown in Table 5 at intervals of $\lambda/2$, calculated between jet extremities.

4.3.6 *Jet equipartition parameters*

The minimum energy density, pressure and magnetic field strength assuming equipartition conditions (i.e. approximately equal energy in the particles and fields) along the jets (see Killeen, Bicknell & Ekers 1986) have been determined using the jet profile data. Although it is unlikely that these conditions hold at all places along the jets, they can be used to estimate the general conditions and trends. Fig. 7 shows the equipartition pressure along the jets. The equipartition energy density and magnetic field strength have similar profiles, as both the equipartition pressure and the energy density are proportional to $(I/\Phi)^{4/7}$, and the equipartition magnetic field strength is proportional to $(I/\Phi)^{2/7}$. The minimum energy density varies[1] in the range $(16\text{–}2.4)\times10^{-13}$ $h^{-4/7}$ J m^{-3} in the north-eastern jet over angular distances of 25–120 arcsec from the core, and in the range $(14\text{–}2.1)\times10^{-13}$ $h^{-4/7}$ J m^{-3} over the same region in the south-western jet. The minimum magnetic field strength lies in the range $(13\text{–}5.1)\times10^{-10}h^{-2/7}$ T in the north-eastern jet over angular distances of 25–120 arcsec from the core, and in the range $(12\text{–}4.7)\times10^{-10}h^{-2/7}$ T over the same region in the south-western jet.

[1]The appropriate SI-to-c.g.s. conversion factors are 1 watt $=10^7$ erg s^{-1}, 1 J m^{-3} $=10$ erg cm^{-3}, 1 pascal $=10$ dyne cm^{-2}, 1 tesla $=10^4$ gauss.

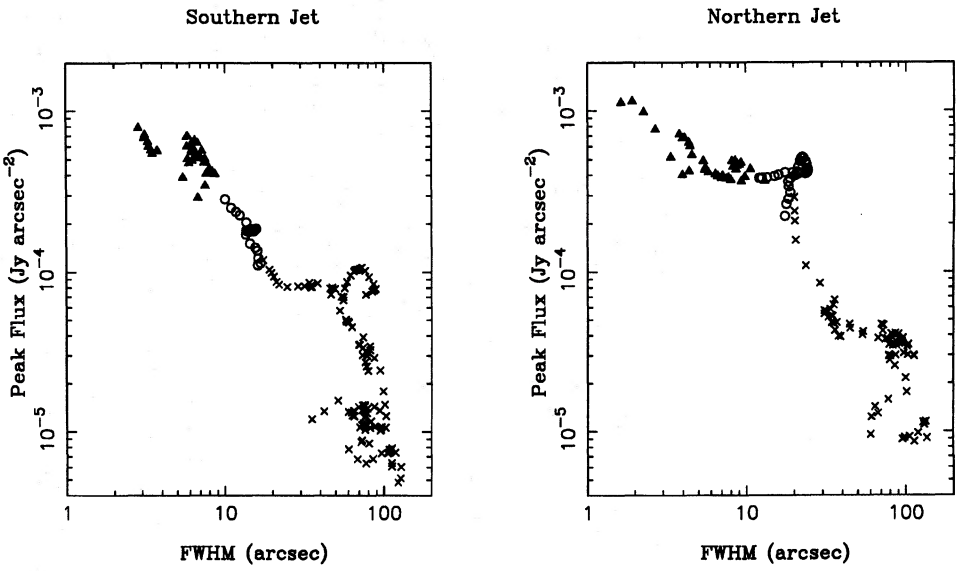

Figure 5. The deconvolved peak surface brightness, I_v (Jy arcsec^{-2}), plotted against the deconvolved full width at half-maximum, Φ (arcsec), in the northern and southern jets. The crosses are derived from the 16 arcsec resolution image, the circles from the 8 arcsec resolution image and the solid triangles from the 4 arcsec resolution image.

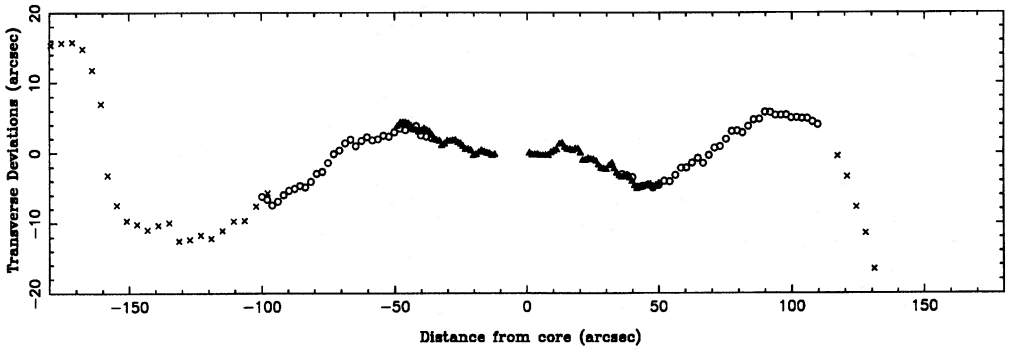

Figure 6. Transverse deviations along the northern jet (positive angular distances from the core) and southern jet (negative angular distances from the core). The crosses are derived from the 16-arcsec image, the circles from the 8-arcsec image and the solid triangles from the 4-arcsec image.

Table 5. Transverse deviations in intervals of $\lambda/2$.

Northern Jet, Θ (arcsec)	λ/R
12–42	18 ± 3
42–95	12 ± 4
95–170	10 ± 2
Southern Jet, Θ (arcsec)	λ/R
12–42	16 ± 2
42–120	24 ± 3
120–152	6 ± 1

4.3.7 Faraday rotation and depolarization

The rotation measures across the jets were calculated from position angles of the electric field vectors from our 8 arcsec resolution data at 4.796 and 8.640 GHz. The rotation measure in the north-eastern jet over angular distances of 1.5–2.5 arcmin from the core is -80 ± 10 rad m^{-2}, while in the south-western jet over the same range it is -60 ± 20 rad m^{-2}. The rotation measure at the core is in the range 300–500 rad m^{-2}.

The depolarization ratio along the jets, deduced from the slice data, does not deviate significantly from unity over the length of the jets.

5 DISCUSSION

5.1 Polarization data

Polarization data on synchrotron radio sources such as radio jets can provide detailed information on the dynamics of the plasma flow. PKS B1318 − 434 exhibits many of the typical configurations of projected magnetic field lines, fractional polarization and total intensity seen in radio jets (e.g. Laing 1981; Bridle & Perley 1984). These include the following.

(1) Magnetic field lines along the jets ($B_\parallel$ configuration) at the base of each jet, $\Theta < 20$ arcsec, indicating strong shear flows along the jet boundary.

(2) Magnetic field lines across the jets ($B_\perp$ configuration) for $\Theta > 20$ arcsec, produced when the jet plasma decelerates and compresses.

(3) The $B_\parallel$ configuration along the edges of outer bends, indicating shearing and/or stretching of magnetic field lines.

(4) The rapid changes in magnetic field structure associated with strong knots in the initial train of bright knots in the northern jet. These are possibly caused by oblique shocks amplifying the magnetic field component parallel to the shock front.

(5) The oscillation of fractional polarization, where a high/low degree of polarization indicates the uniformity/non-uniformity of the projected magnetic field lines along the line of sight and whether the flow is laminar/turbulent. The transition of high to low fractional polarization is associated with hotspots.

(6) High fractional polarization and projected magnetic field lines along the sides of the lobes, caused by compression of the lobe plasma by collision with the external medium.

Comparison of detailed jet polarization data with numerical models, such as the force-free equilibria ($\boldsymbol{J} \times \boldsymbol{B} = \boldsymbol{0}$) in magnetized jets (Königl & Choudhuri 1985), has been made by Jackson et al. (1990). In their model the observed magnetic fields and total intensity knots and wriggles are due to the projection of a jet, inclined to the line of sight, on to the plane of the sky. They present total intensity and magnetic field images that show many of the features seen in our data; in particular, for a pure helical mode they show magnetic field lines that are directed around knots and stronger polarization on one side of the jet. This configuration closely matches our 4 arcsec resolution data on the north-eastern jet.

5.2 Faraday rotation and depolarization

Faraday rotation in the absence of depolarization can indicate that the rotation is due to an intervening homogeneous magneto-ionic screen. This foreground screen may be surrounding the radio galaxy, whereby a gradient in the rotation measure across the source may be seen if the jets are inclined at an angle to the observer. Interpretation of the rotation measure is complicated without detailed knowledge of the three-dimensional structure of the jet, and the distribution of plasma and magnetic fields.

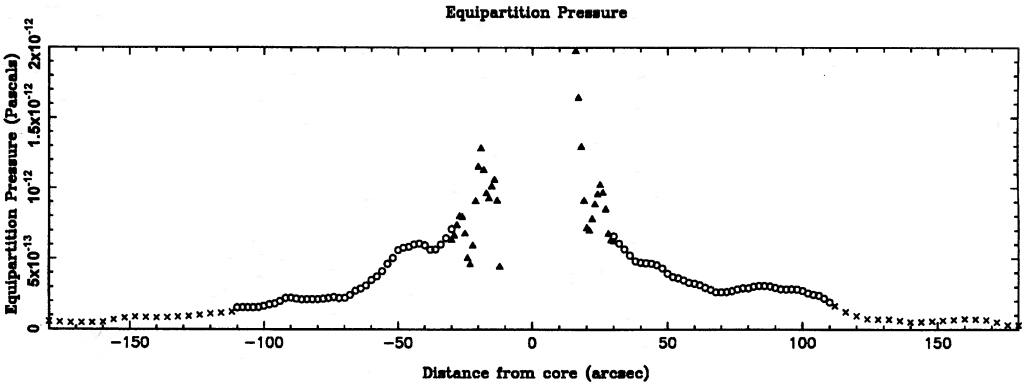

Figure 7. Equipartition pressure along the northern jet (positive angular distances from the core) and southern jet (negative angular distances from the core). The crosses are derived from the 16 arcsec resolution image, the circles from the 8 arcsec resolution image and the solid triangles from the 4 arcsec resolution image.

PKS B1318 − 434 lies behind the southern lobe of Centaurus A (1322 − 4248, NGC 5128). The rotation measure across Centaurus A is -56 ± 1 rad m^{-2} (Simard-Normandin, Kronberg & Button 1981), and does not vary greatly from this value across the lobes of Centaurus A as a whole (Junkes et al. 1993). As this is a global value, a small amount of Faraday rotation may be attributed to Centaurus A itself, but it is mostly due to our Galaxy. For our rotation measure measurements of -80 ± 10 and -60 ± 20 rad m^{-2} over the region $1.5 < \Theta < 2.5$ arcmin in the northern and southern jets respectively, the rotation measures intrinsic to the jets in PKS B1318 − 434 are small, -24 ± 10 and -4 ± 20 rad m^{-2} respectively.

5.3 Jet transverse deviations

Dominant features of the radio structure visible on total intensity images at all resolutions are the large transverse deviations which have a strong inversion symmetry about the core along its entire length. Many ideas have been put forward to explain the mechanism by which this type of inversion symmetry is produced. It may be caused by the precession of the central collimator, by magnetic or surface instabilities or by changing conditions within the galaxy. The presence of NGC 5091 and, as already noted, the fact that its orbital plane about NGC 5090 is perpendicular to the radio jet axis strongly suggest that it may play a part in this aspect of the jet structure.

At distances close to the core, the wavelengths of the jet deviations are small. As the jets propagate outward, the wavelength increases, but this is not indicative of a decelerating jet with a structure dominated by the precession of the central collimator. This may be evidence for jet acceleration caused by the buoyant force of a light jet (compared with the surrounding environment) under the influence of pressure gradients in the galactic atmosphere.

Wirth, Smarr & Gallager (1982), in a study of dumbbell galaxies, suggest mechanisms that cause the precession of radio jets by an encounter with a nearby galaxy in terms of tidal distortion of the interstellar mass distribution. It is assumed that the direction of the jet responds to these distortions or pressure gradients by refracting through this environment. In one mechanism, the torque imposed on the interstellar medium of the radio galaxy by the companion galaxy will move the rotation axis, and therefore the radio axis, by $\theta \sim \varepsilon(R/r)(V_0/V_r)(M/m)$, where ε is the ellipticity and R the radius of the jet-confining gas cloud attached to the radio galaxy of mass m, with rotational velocity V_r. The companion galaxy is at a distance of r and has a mass of M and orbital velocity V_0. The interstellar medium at different galactic radii will precess at different rates, producing radio jets that appear to precess, possibly over many periods. Applying this simple model to NGC 5090/5091, we assume an equal mass for each galaxy. We take velocity measurements of the central regions of NGC 5090 from SB, where $V_r = 80$ km s^{-1} within a galactic radius of 7 arcsec of ellipticity 0.15, the galactic redshift difference to be the orbital velocity, $V_0 = 245$ km s^{-1}, and the galactic nuclei to be approximately 105 arcsec apart. These give an opening angle for the transverse deviations of approximately 4°, comparable to the observed transverse deviation opening angle over the first 3 arcmin of 11°. Another possibility is that the encounter may provide the initial perturbing conditions from which jet surface instabilities amplify.

The radio axis of PKS B1318 − 434 is not closely aligned with the minor axis of the elliptical galaxy (position angle 2°). Galactic rotation curves at core radii less than 7 arcsec ($1.2\,h^{-1}$ kpc; see SB) show that the galaxy rotates about the major axis. This may account for the misalignment if the jets are formed along this spin axis. On a larger scale, White, McAdam & Jones (1984) discuss possible relationships between radio and optical axes in the NGC 5090/5091 system and Centaurus A.

In the extremities of the source, the elongated lobes will tend to bend toward regions of low pressure if the jet is still buoyant, corresponding to the minor axis of the pressure distribution (Henriksen, Vallée & Bridle 1981). This is clearly seen in the bending of the northern lobe towards the north at its end. Also, the northern jet/lobe appears to meander to a greater degree than the southern jet/lobe, which may be evidence for a lower flow velocity.

5.4 Laminar jet adiabats

The laminar jet adiabats describe the intensity–radius evolution along the jet (Bridle et al. 1991). The assumptions made in their derivation are that magnetic flux is conserved, that radiating particles do work as the jet radius expands and respond to variations in the flow velocity, that there is no particle re-acceleration, that the jet is optically thin and that the relativistic electron energy distribution is a power law.

For a spectral index of $\alpha = 0.7 \pm 0.2$, the peak flux of a $B_{\parallel}$-dominated jet is given by $I \propto \Phi^{-5.3\pm0.7} v^{-1.5\pm0.1}$, and that for a $B_{\perp}$-dominated jet is given by $I \propto \Phi^{-3.6\pm0.5} v^{-3.2\pm0.3}$. For a constant-velocity, expanding jet our jet data do not match the laminar jet adiabats at any point along its length, indicating that there is rapid deceleration along the jet or that the flow is non-laminar.

5.5 Estimation of the jet thermal density

The density of thermal material, n_e, can be estimated by studying the frequency dependence of fractional polarization. Current theory on the interpretation of fractional polarization and depolarization is limited because of the lack of knowledge of the exact distribution of plasma and structure of the magnetic fields within a radio source. In the case of a uniform magnetic field and a cylindrical jet of homogeneously distributed plasma, an upper limit on the thermal number density can be made assuming that all depolarization occurs within the jet (Burns, Feigelson & Schreier 1983). The Faraday depth is given by $F = 1600 n_e B_{\parallel} \lambda^2 D$, where the magnetic field strength parallel to the line of sight $B_{\parallel}$ is in μgauss, the observing wavelength λ is in m and D is the diameter of the cylinder in kpc. A lower limit on the Faraday depth can be determined from measurements of the fractional polarization or depolarization ratio for this configuration.

From our observations of PKS B1318 − 434, the upper limits on the thermal number density under equipartition conditions, based on fractional polarization measurements at 4.796 GHz, range from 0.1 cm^{-3} at $\Theta = 18$ arcsec to approximately 0.03 cm^{-3} at $\Theta = 90$ arcsec in both jets, while densities based on depolarization measurements are approximately one-fifth of these.

5.6 Mach number estimation

5.6.1 Mach number from transverse deviations

In a study of the spatial stability of jets, Hardee (1987) has calculated the resonant wavelengths of fundamental instability modes. For a helical oscillation ($n = 1$), the fastest growing oscillation or resonant wavelength is related to simple quantities by the equation $\lambda_h / R \approx 5.2M/(0.66 + \eta^{1/2})$ at high Mach number (λ_h is the wavelength of the helical oscillation, R the jet radius, M the Mach number and $\eta = \rho_{jet}/\rho_{external}$ the jet density ratio). For a light jet (i.e. $\eta \rightarrow 0$) and provided that the observed jet deviations are the resonant oscillation, the Mach number may be estimated.

For the northern jet of PKS B1318 − 434 this gives Mach numbers of 2.2 ± 0.3 at the base of the jet and 2.0 ± 0.6 just before entering the lobe. Similarly, for the southern jet, Mach numbers of 2.0 ± 0.2 at the jet base and 3.0 ± 0.3 at its end are obtained.

5.6.2 Mach number from knot spacings

The Prandlt formula, $\lambda_k / R = 2.61(M^2 - 1)^{1/2}$, can be used to estimate the Mach number, M, from the knot separation, λ_k. This formula is applicable provided that the shocks are mild and not in the saturation regime, where $\lambda_k / R \approx 4$.

Our data show that $\lambda_k / R = 2.7 \pm 0.9$ and $\lambda_k / R < 2.9 \pm 0.7$ over the train of knots in the north-eastern and south-western jets respectively, less than 40 arcsec from the core. This corresponds to Mach numbers of 1.5 ± 0.3 and 1.5 ± 0.2.

5.6.3 Mach number in oblique shocks

Side-to-side edge brightening has been seen in high-resolution observations of the inner radio jet of Centaurus A (Clarke, Burns & Feigelson 1986). One interpretation of this structure is that it is produced by internal oblique shocks and/or shocks from the interaction between the jet and the interstellar medium. Our highest resolution image shows that some knots are not aligned in a straight line, although they do not appear edge-brightened at this resolution. If these deviations can be attributed to oblique shocks, the bulk flow Mach number is given by $M = [0.8(P_2/P_1) + 0.2]^{1/2} (\sin\theta)^{-1}$ where $P_1(P_2)$ is the pressure before (after) the shock and θ is the bending or deviation angle. Under equipartition conditions $P_2/P_1 = (I_2/I_1)^{4/7}$, where $I_1(I_2)$ is the flux density before (after) the shock.

We do not have high enough resolution to determine I_2/I_1 accurately, but the assumption that it is close to unity, so that the bending angle essentially reduces to the Mach angle, yields a bulk flow Mach number of ~ 4 in the southern jet at the $B_{\parallel}$-to-$B_{\perp}$ transition point ($\Theta = 18$ arcsec) with a bending angle of 14°.

5.6.4 Mach number from spreading rate

For an unconfined or free adiabatically expanding jet, the Mach number can be estimated from $d\Phi/d\Theta = (2/M) \sec i$, where i is the inclination angle. It is clear (from the low spreading rate) that both jets are confined over most of their length, as commented upon earlier. However, if we take the region over which the jets are expanding most rapidly to represent a free jet, then we obtain a lower limit on the

Table 6. Mach number summary.

Method	Range (arcsec)	Mach number
Transverse deviations	north 12–42	2.2 ± 0.3
	south 12–42	2.0 ± 0.2
	north 42–95	2.0 ± 0.6
	south 42–120	3.0 ± 0.3
Knot spacings	north 12–40	1.5 ± 0.3
	south 12–40	1.5 ± 0.2
Oblique shocks	south 18	~4
Spreading rate	north 55–75	> 3.1

Mach number of $M=3.1$ in the northern jet over the range $55<\Theta<75$ arcsec.

A summary of Mach numbers obtained from the above methods is shown in Table 6.

5.7 Jet velocity estimation

5.7.1 *Jet velocity from energy budget*

If the thermal particle contribution to the jet pressure can be neglected then the velocity of the jet can be estimated from the lobe and jet energetics. The energy flux along a jet for a hot, light jet with a top-hat profile is given by (Bicknell 1986)

$$F_e \approx \frac{4\pi}{3}\Phi^2 vP\left(1+\frac{1}{6}M^2\right),$$

where Φ is the jet FWHM, v the velocity, P the pressure and M the Mach number. The energy flux along the jet derived under equipartition conditions (Bridle et al. 1991) for a top-hat jet is

$$F_e \approx \frac{34\pi}{13\sqrt{3}}\Phi^2 vP\left(1+\frac{13M^2}{51}\right).$$

The energy flux at any point along a jet is

$$F_e(z)=\kappa^{-1}L_{\rm lobe}+L_{\rm jet}(z)-F_e^{\rm ent}(z),$$

where $L_{\rm jet}$ is the jet total luminosity, $F_e^{\rm ent}(z)$ is the entrained energy flux between the point z and the lobe, $L_{\rm lobe}$ is the lobe total luminosity and $\kappa=\tau/t_{\rm rad}$, the age of the source τ as a fraction of its radiative lifetime $t_{\rm rad}$. The parameter κ can be estimated from reliable spectral gradients across the lobe, but this estimation is complicated without detailed knowledge of the mixing processes occurring there. For a jet that remains hot with respect to the surrounding environment, the entrained energy flux can be neglected.

Using the equipartition pressure, an upper limit on the jet velocity can be obtained. The velocity estimates for the northern and southern jets, using the method of Bicknell, for typical values of Mach number and κ are shown in Table 7. The errors in velocity estimates are approximately 10–20 per cent. Velocity estimates using the method of Bridle et al. are 20–40 per cent greater than these. These velocity estimates may be biased if the jet is not in equipartition or the entrained energy flux is significant. Jet modelling is required to calculate the entrained energy flux, and therefore to estimate the jet properties better, which we do not carry out in this paper.

5.7.2 *Velocity estimates from spectral index variations*

The jet velocity may be estimated from the synchrotron ageing seen as spectral index gradients along the jets. The models most commonly used are based on the change of the electron energy distribution, initially from a power-law distribution,

$$N(E)=N_0E^{-\gamma}$$

to

$$N(E,\phi,t)=N_0E^{-\gamma}[1-C_2Et(B^2\sin^2\phi)]^{\gamma-2}$$

over time t, where ϕ is the pitch angle, C_2 is a constant and B is the magnetic field strength (Pacholczyk 1970). The Kardashev–Pacholczyk (KP) model assumes that electron orbits maintain a constant pitch angle, while the Jaffe–Perola (JP) model makes a more realistic assumption that the pitch angle distribution is isotropic on time-scales less than the radiative lifetime. These models have been used to calculate separation velocities between hotspots in lobes and the lobes themselves (Myers & Spangler 1985). Tribble (1993) extends the KP and JP models by considering synchrotron ageing in the presence of random magnetic fields.

The jet velocities implied by our spectral index data assume that there is no particle re-acceleration within the selected angular distances. For the relatively small spectral gradients seen in our spectral index data, the KP and JP model jet velocity estimates in a random magnetic field, given by Tribble, lie within the KP and JP model jet velocity estimates for a uniform field, given by Myers & Spangler. We therefore quote velocities for the latter as upper and lower limits. From our 8 arcsec resolution data, velocities for the KP and JP models in the northern jet, in the range $20<\Theta<35$ arcsec, are 560 and 510 $h^{-4/7}$ km s^{-1} respectively; for the range $48<\Theta<65$ arcsec the velocities are 370 and 320 $h^{-4/7}$ km s^{-1}. In the southern jet, in the range $65<\Theta<82$ arcsec, velocities for the KP and JP models are 410 and 320 $h^{-4/7}$ km s^{-1} respectively.

Using the spectral index gradients from our 16 arcsec resolution data where we have better (u,v) coverage and more closely matched (u,v) spacings, slightly higher velocities are implied. Velocity estimates, using our 16 arcsec resolution data, for the KP and JP models in the northern jet, in the range $45<\Theta<60$ arcsec, are 1900 and 1000 $h^{-4/7}$ km s^{-1}; in the range $95<\Theta<115$ arcsec the velocities are 680 and 510 $h^{-4/7}$ km s^{-1}. In the southern jet, in the range $28<\Theta<53$ arcsec, velocities for the KP and JP models are 1300 and 980 $h^{-4/7}$ km s^{-1} respectively; in the range $65<\Theta<120$ arcsec the velocities are 670 and 640 $h^{-4/7}$ km s^{-1}.

Table 7. Velocity estimates from energy budget considerations using several values for the Mach number and κ.

Angular distance from the core	M=1, κ=0.1 Velocity (km s^{-1})	M=2, κ=0.1 Velocity (km s^{-1})	M=1, κ=0.05 Velocity (km s^{-1})	M=2, κ=0.05 Velocity (km s^{-1})
north-east jet 15″	26,000	18,000	50,000	35,000
north-east jet 120″	2,000	2,000	5,000	3,000
south-west jet 15″	26,000	18,000	52,000	36,000
south-west jet 120″	5,000	4,800	11,000	7,000

Estimates of the jet velocity using this method are approximately a factor of 10 less than those using the energy budget. These estimates will be biased if we are missing significant flux because of a lack of adequate (u, v) coverage and/or the spectral index gradients are representative not of the bulk flow electron energy distribution, but of a surrounding boundary layer medium.

6 SUMMARY

This paper has presented 4.796-GHz total intensity and polarization images at resolutions of 4, 8 and 16 arcsec of the radio jets in the galaxy NGC 5090 (PKS B1318 − 434). The main features of these images are the following.

(1) The north-eastern jet 'turns on' at an angular distance of 15 arcsec (2.5 h^{-1} kpc); prior to this it is faint and unresolved, and has magnetic field lines directed along the jet. The projected magnetic field vectors fluctuate backwards and forwards across the jet over the range $20 < \Theta < 55$ arcsec and are more highly polarized on the western side of the jet. In the section where $55 < \Theta < 120$ arcsec the configuration of projected magnetic field vectors and the bending in the jet give the impression of a jet looping over itself, seen in projection. The north-eastern lobe is diffuse and elongated; the projected magnetic field lines are perpendicular to the ridge line and parallel to the lobe surface near the boundary.

(2) The south-western jet is not detected at angular distances less than 12 arcsec. After this point, the jet flares into a train of bright knots. The magnetic field lines are parallel to the jet over the first two knots, and then become perpendicular to the jet and remain so over the rest of the jet. The elongated south-western lobe is initially bright with high fractional polarization and projected magnetic field lines aligned with the sides in several areas along the lobe boundary.

(3) The transverse deviations have strong 'S' inversion symmetry.

(4) The surface brightness of the jets after they flare is symmetric, although on the scale of the whole source the surface brightness appears asymmetric.

(5) Correlations of total intensity, fractional polarization and spectral index show the following trends: high fractional polarization and steep spectral indices are associated with knots, or appear just before a knot, and lower fractional polarization and flatter spectral indices appear after a knot or group of knots.

(6) The jets are not depolarized, and the Faraday rotations intrinsic to the jets at angular distances of 1.5–2.5 arcmin from the core are -24 ± 10 and -4 ± 20 rad m^{-2} for the northern and southern jets respectively. A high rotation measure (300–500 rad m^{-2}) in the core is evidence for large amounts of magneto-ionic material there.

(7) The jet Mach number has been estimated using a number of methods. Mach numbers are typically 1–3.

(8) The jet velocity has been estimated from spectral index variations and from the source energy budget. From the energy budget we expect mildly relativistic velocities of 0.05–0.2 times the speed of light just after the jets flare. However, velocities along the bulk of the jets are typically 2000–15 000 km s^{-1}.

ACKNOWLEDGMENTS

We acknowledge a University of Western Sydney Nepean Seed Grant and the Australian Research Council (ARC) for initial financial support in this project, and the ATNF for the use of their facilities and assistance. We thank Graeme White and Martin Anderson for help with the observations. BDL thanks Geoff Bicknell, on a visit to the ANUATC, and Graeme White for useful suggestions, and also acknowledges support from a Nepean Postgraduate Research Award.

REFERENCES

Bergwall N. A. S. et al., 1978, A&AS, 33, 243
Bicknell G. V., 1986, ApJ, 300, 591
Bridle A. H., Perley R. A., 1984, ARA&A, 22, 319
Bridle A. H., Baum S. A., Fomalont E. B., Fanti R., Parma P., Ekers R. D., 1991, A&A, 245, 371
Burns J. O., Feigelson E. D., Schreier E. J., 1983, ApJ, 273, 128
Clarke D. A., Burns J. O., Feigelson E. D., 1986, ApJ, 300, L41
Cooper B. F. C., Price R. M., Cole D. J., 1965, Aust. J. Phys., 18, 586
Ekers J. A., ed., 1969, Aust. J. Phys. Astrophys. Suppl., 7, 1
Hardee P. E., 1987, ApJ, 313, 607
Henriksen R. N., Vallée J. P., Bridle A. H., 1981, ApJ, 249, 40
Jackson N., Browne I. W. A., Shone D. L., Lind K. R., 1990, MNRAS, 244, 750
Jones P. A., McAdam W. B., 1992, ApJS, 80, 137
Jones P. A., McAdam W. B., Reynolds J. E., 1994, MNRAS, 268, 602
Junkes N., Haynes R. F., Harnett J. I., Jauncey D. L., 1993, A&A, 269, 29
Killeen N. E. B., Bicknell G. V., Ekers R. D., 1986, ApJ, 302, 306
Königl A., Choudhuri A. R., 1985, ApJ, 289, 173
Laing R. A., 1981, ApJ, 248, 87
Myers S. T., Spangler S. R., 1985, ApJ, 291, 52
Pacholczyk A. G., 1970, Radio Astrophysics. Freeman, San Francisco
Schilizzi R. T., 1975, Mem. R. Astron. Soc., 79, 75
Schilizzi R. T., McAdam W. B., 1975, Mem. R. Astron. Soc., 79, 1
Simard-Normandin M., Kronberg P. P., Button S., 1981, ApJS, 45, 97
Slee O. B., Sadler E. M., Reynolds J. E., Ekers R. D., 1994, MNRAS, 269, 928
Smith R. M., Bicknell G. V., 1986, ApJ, 308, 36 (SB)
Tribble P. C., 1993, MNRAS, 261, 57
Wall J. V., Schilizzi R. T., 1979, MNRAS, 189, 593
White G. L., McAdam W. B., Jones I. G., 1984, Proc. Astron. Soc. Aust., 5, 507
Wirth A., Smarr L., Gallagher J. S., 1982, AJ, 87, 602